Ab initio density functional studies of transition-metal sulphides: I. Crystal structure and cohesive properties

1997 J. Phys.: Condens. Matter 9 11085

(http://iopscience.iop.org/0953-8984/9/50/013)

J. Phys.: Condens. Matter **9** (1997) 11085–11106. Printed in the UK PII: S0953-8984(97)83862-3

Ab initio density functional studies of transition-metal sulphides: I. Crystal structure and cohesive properties

P Raybaud†‡, G Kresse†, J Hafner† and H Toulhoat‡

† Institut für Theoretische Physik, and Centre for Computational Material Science, Technische Universität Wien, Wiedner Hauptstraße 8–10, A-1040 Wien, Austria

‡ Institut Français du Pétrole, Groupe de Modélisation Moléculaire, BP 311, F-92852 Rueil-Malmaison, France

Received 30 April 1997

Abstract. The structural and cohesive properties of more than thirty transition-metal sulphides of various stoichiometries and crystal structures have been investigated using density functional theory, with the aim of establishing a correlation between the strength of the metal–sulphur bond and the catalytic activities of these materials. It is shown that the local density approximation has a tendency to overestimate the strength of the bonding. The overbinding manifests itself in the prediction of too small atomic volumes and too large cohesive energies. Non-local corrections to the local exchange–correlation functional in the form of a generalized-gradient approximation correct the overbinding (albeit with a certain tendency to overcorrect, especially for the sulphides of the heavy transition metals) and result in accurate structural prediction and cohesive energies. A correlation between the sulphur–metal bond strength and the catalytic activities is established.

1. Introduction

Transition-metal sulphides (TMS) play an important role as catalysts in the petroleum-refining industry. TMS represent the only known class of stable catalytically active phases for strongly sulpho-reductive hydroprocessing conditions. The highest catalytic activity has been measured for the pyrite-type disulphides RuS_2, OsS_2, IrS_2 [1, 2] but most industrially used hydroprocessing catalysts are mixed sulphides of the type Co(Ni)–Mo(W)S with the layered MoS_2 structure, supported on alumina. These systems are used because they represent a synergetic effect, i.e. the mixed sulphide is much more active than each of the monometallic sulphides [3]. As these mixed sulphides involve relatively low-cost metals, they also represent the best activity/cost ratio. An enormous research effort has been directed towards obtaining a fundamental understanding of the variation of the catalytic activity in the series of the TMS, but it seems fair to say that no convincing picture has emerged yet: according to Nørskov *et al* [4] the catalytic activity should be inversely correlated with the metal–sulphur bond strength with bond strength estimated in terms of a semiempirical approach based on the bulk modulus of the metal and the strength of the TM d/S p hybridization. On the other hand Toulhoat *et al* [5] have redefined bond strength as the cohesive energy of the TMS per TM–S bond and pointed out that TMS with TM–S bond strengths that are too low or too high are practically inactive, whereas the catalytically active TMS are those with intermediate TM–S bond strength. This interpretation would be in the spirit of the Sabatier principle [6, 7] which states that if the heat of formation of the compound is too large, the rate of the reaction will also be small, because it is

0953-8984/97/5011085+22$19.50

controlled by the rate of decomposition of a too stable compound. On the other hand if the heat of formation is small, the affinity between the catalyst and reactant will also be weak and the reaction rate small as it is controlled by the formation of the compound [7]. Such a correlation offers a key to the understanding of the synergetic effect: in the mixed Co(Ni)–Mo(W)S sulphides, the 3d sulphides of Co and Ni have low TM–S bond strength, while the 4d sulphides have high TM–S bond strength. Although the precise local structure of the mixed sulphides is still unknown, it seems legitimate to assume that two metals sharing the same sulphur anion will achieve the intermediate bond-strength characteristic for the catalytically active phases. However, there is still a long way to go from this correlation to a fundamental understanding of the factors influencing the catalytic processes.

In this paper we present a comprehensive study of the cohesive and structural properties of a wide series of TMS within local density functional (LDF) theory [8, 9]. A companion paper will present the corresponding results on the electronic structure. In our view these results represent the first step towards a quantum-mechanical calculation of the properties of TMS surfaces and the modelling of elementary processes relevant to catalysis.

Our paper is organized as follows. In section 2 we review very briefly the technique used for the solution of the Kohn–Sham equations and for the calculation of the total energies and interatomic forces. In section 3 we review the TMS covered by this study and describe very briefly their crystal structures. Section 4 describes the results of optimization of the crystalline structures: ionic coordinates and the volume and shape of the unit cell are optimized simultaneously under the constraints of a fixed space group symmetry. As the local density approximation (LDA) to density functional theory (DFT) tends to overestimate the strength of the chemical bond, we have explored non-local corrections to the exchange–correlation functional in the form of generalized-gradient approximations [10]. Trends in the cohesive energies as presented in the LDA and GGA are discussed in section 5, together with structural phase stability, concentrating on the important aspect of the relative stability of the pyrite and layered (MoS_2-type) structures among the disulphides and the relative stability of sulphides of different stoichiometry, as determined by the composition dependence of the heats of formation.

2. Theory

2.1. Variational solution of the Kohn–Sham equations and structural optimization

For our calculations we used the Vienna *ab initio* simulation program VASP [11–14] based on the following principles.

(1) Electronic exchange and correlation are treated in the local density approximation (LDA) [8, 9]. We used the exchange–correlation functional based on the quantum Monte Carlo calculations of Ceperley and Alder as parametrized by Perdew and Zunger [15]. Non-local corrections are introduced in the form of the generalized-gradient expansion proposed by Perdew *et al* [10]. To improve the convergence of Brillouin-zone integrations we used for metallic systems techniques based on a smearing of the one-electron levels. Formally, the smearing methods may be cast into the form of a finite-temperature DFT [16] where the electronic free energy is the variational quantity.

(2) The calculations are performed in a plane-wave basis. The electron–ion interaction is described by fully non-local optimized ultrasoft pseudopotentials similar to those introduced by Vanderbilt [17, 18]. Extensive tests of the ultrasoft pseudopotentials for transition metals have been described in references [19, 20].

(3) The minimization of the electronic free energy is performed using an efficient iterative matrix-diagonalization routine based on a sequential band-by-band residuum minimization method (RMM) [13, 14, 21]. Alternatively, a matrix diagonalization based on preconditioned band-by-band conjugate-gradient (CG) minimization has been used [11, 12, 22, 23]. An improved Pulay mixing [13, 24] has been used to update the charge density and potential.

(4) The optimization of the atomic geometry (ionic coordinates, volume and shape of the unit cell) is performed via a conjugate-gradient minimization of the total energy, using the Hellmann–Feynman forces on the atoms and stresses on the unit cell.

For a more detailed description of the technique, we refer the reader to the papers by Kresse *et al* [12–14].

2.2. Technical aspects of the calculations

The ultrasoft pseudopotentials have been constructed on the basis of scalar relativistic solutions for atomic $d^{n-1}s^1$ (n = group number) reference configurations. All three angular-momentum components of the pseudopotential were described by ultrasoft pseudopotentials, with reference energies chosen such as to span the approximate width of the occupied bands. The cut-off radii for the pseudo-wavefunctions vary between 2.58 au and 2.43 au for the 3d metals; the augmentation radii for the d augmentation charges vary between 2.10 au and 1.98 au. The cut-off radii and radii for the augmentation charges of the 4d and 5d metals increase essentially in proportion to the Wigner–Seitz radii of the elements. The all-electron potential truncated at a radius varying between 1.77 au and 1.67 au for the 3d metals was chosen as the local pseudopotential. Again a larger radius was chosen for the 4d and 5d metals. Typical cut-off energies for the plane-wave expansion of the eigenstates can be as low as 250 eV, as confirmed by detailed convergence tests and comparisons with all-electron calculations [20]. For S the atomic reference configuration was s^2p^4; only the s and p components were described by ultrasoft pseudopotentials, and the d component was modelled by a norm-conserving potential. All of the pseudopotentials were generated in the LDA. Gradient corrections were applied only in the solid-state calculations.

During the geometry optimizations, $\boldsymbol{k}$-point grids varying from $2 \times 2 \times 2$ to $4 \times 4 \times 4$ (depending on the size of the unit cell) have been used for Brillouin-zone integrations. For semiconductors, the linear tetrahedron method with Blöchl corrections [25, 27] was used. For metallic systems we used the Methfessel–Paxton [26] technique with a smearing of $\sigma = 0.4$ eV in order to minimize errors in the Hellmann–Feynman forces due to the entropic contribution to the electronic free energy [13, 14]. In the final iterations for the optimized structure the $\boldsymbol{k}$-point grid was extended to $8 \times 8 \times 8$ and the tetrahedron method was used to achieve total energies converged with respect to the Brillouin-zone integrations.

The calculations described here have been performed for the paramagnetic state of the TMS (we shall briefly comment on cases where magnetic effects can be of importance for the cohesive and structural properties). Spin-polarization effects are, however, important for describing the correct ground state of the free transition-metal atoms. We have again used VASP to perform spin-polarized calculations of the total energies and magnetic moments of the free atoms, both within the LDA and GGA, placing the atom at the centre of a large box. Details of these calculations will be described elsewhere [28]. The total energies of the spin-polarized atoms have been used in the calculation of the cohesive energies of the TMS.

Table 1. Crystallographic data for transition-metal sulphides: structure type, symmetry, lattice parameters (in Å), and partial coordination numbers Z_{MS} (M = metal, S = sulphur).

	Compound (structure prototype)	Reference	Bravais class	Space group*	*a*	*b*	*c*
3d	VS (NiAs)	[29]	Hexagonal	$P6_3/mmc$ (194)	3.340	3.340	5.785
	CrS (NiAs)	[30]	Hexagonal	$P6_3/mmc$ (194)	3.439	3.439	5.324
	Cr_2S_3	[31]	Trigonal	$R\bar{3}$ (148)	5.937	5.937	16.698
	MnS (NaCl)	[32]	Cubic	$Fm\bar{3}m$ (225)	5.240	5.240	5.240
	MnS_2 (FeS_2)	[33]	Cubic	$Pa\bar{3}$ (205)	6.091	6.091	6.091
	FeS (NiAs)	[34]	Hexagonal	$P6_3/mmc$ (194)	3.445	3.445	5.763
	FeS (troilite)	[35]	Hexagonal	$P\bar{6}2c$ (190)	5.958	5.958	11.740
	FeS_2 (pyrite)	[36]	Cubic	$Pa\bar{3}$ (205)	5.428	5.428	5.428
	FeS_2 (marcasite)	[37]	Orthorhombic	$Pnnm$ (58)	4.436	5.414	3.381
	Co_9S_8	[38]	Cubic	$Fm\bar{3}m$ (225)	9.928	9.928	9.928
	CoS (NiAs)	[39]	Hexagonal	$P6_3/mmc$ (194)	3.370	3.370	5.528
	CoS_2 (FeS_2)	[40]	Cubic	$Pa\bar{3}$ (205)	5.539	5.539	5.539
	Ni_3S_2	[41]	Trigonal	$R32$ (155)	5.730	5.730	7.12
	NiS (NiAs)	[30]	Hexagonal	$P6_3/mmc$ (194)	3.439	3.439	5.324
	NiS (millerite)	[42]	Trigonal	$R3m$ (160)	9.589	9.589	3.165
	NiS_2 (FeS_2)	[43]	Cubic	$Pa\bar{3}$ (205)	5.620	5.620	5.620
4d	NbS (NiAs)	[44]	Hexagonal	$P6_3/mmc$ (194)	3.320	3.320	6.460
	NbS_2 (MoS_2)	[45]	Hexagonal	$P6_3/mmc$ (194)	3.310	3.310	11.890
	MoS_2	[46]	Hexagonal	$P6_3/mmc$ (194)	3.160	3.160	12.294
	TcS_2	[47]	Triclinic	$P\bar{1}$ (12)	6.659	6.375	6.465
	RuS_2 (FeS_2)	[48]	Cubic	$Pa\bar{3}$ (205)	5.611	5.611	5.611
	Rh_2S_3	[49]	Orthorhombic	$Pbcn$ (60)	8.462	5.985	6.138
	PdS	[50]	Tetragonal	$P4_2/m$ (84)	6.429	6.429	6.611
	PdS_2	[51]	Orthorhombic	$Pbca$ (61)	5.460	5.541	7.531
5d	TaS_2 (MoS_2)	[52]	Hexagonal	$P6_3/mmc$ (194)	3.314	3.314	12.097
	WS_2 (MoS_2)	[53]	Hexagonal	$P6_3/mmc$ (194)	3.153	3.153	12.323
	ReS_2	[54]	Triclinic	$P\bar{1}$ (12)	6.417	6.377	6.461
	OsS_2 (FeS_2)	[55]	Cubic	$Pa\bar{3}$ (205)	5.619	5.619	5.619
	Ir_2S_3	[49]	Orthorhombic	$Pbcn$ (60)	8.465	6.011	6.149
	IrS_2 (FeS_2)	[56]	Cubic	$Pa\bar{3}$ (205)	5.680	5.680	5.680
	PtS	[57]	Tetragonal	$P4_2/mmc$ (131)	3.470	3.470	6.100

3. Systems studied

Table 1 summarizes the crystallographic information on the known TMS. In addition to the composition, the space group symmetry and the lattice parameters, we list the metal–sulphur, sulphur–metal, metal–metal, and sulphur–sulphur coordination numbers. We note that direct metal–metal neighbours exist in Cr_2S_3, the troilite form of FeS, in Co_9S_8, Ni_3S_2 and in the millerite form of NiS. Direct sulphur neighbours exist only in the pyrite and marcasite structures in the form of S pairs. For the monosulphides, the most important crystal structure is the NiAs type assumed by a number of 3d monosulphides (VS, CrS, FeS, CoS, NiS) and by NbS. Among the disulphides, the dominant structure types are the pyrite structure formed by the 3d disulphides MnS_2, FeS_2, CoS_2 and NiS_2, as well as by the 4d compounds RuS_2 and RhS_2 and the 5d compounds OsS_2 and IrS_2, and the layered MoS_2-type structure which is stable for the 4d and 5d disulphides NbS_2, MoS_2, TaS_2, WS_2. For the layered disulphides, variations of the stacking sequence and registry of successive S–TM–S sandwiches along the axis perpendicular to the layers lead to a number of polytypes

Table 1. (Continued)

Compound (structure prototype)		Z_{MS}	Z_{SM}	Z_{MM}	Z_{SS}
3d	VS (NiAs)	6	6	0	0
	CrS (NiAs)	6	6	0	0
	Cr_2S_3	6	4	0–1–2	0
	MnS (NaCl)	6	6	0	0
	MnS_2 (FeS_2)	6	3	0	1
	FeS (NiAs)	6	6	0	0
	FeS (troilite)	6	6	4	0
	FeS_2 (pyrite)	6	3	0	1
	FeS_2 (marcasite)	6	3	0	1
	Co_9S_8	6–7	4–5	0–3	0
	CoS (NiAs)	6	6	0	0
	CoS_2 (FeS_2)	6	3	0	1
	Ni_3S_2	4	6	4	0
	NiS (NiAs)	6	6	0	0
	NiS (millerite)	6	6	2	0
	NiS_2 (FeS_2)	6	3	0	1
4d	NbS (NiAs)	6	6	0	0
	NbS_2 (MoS_2)	6	3	0	0
	MoS_2	6	3	0	0
	TcS_2	6	3	0	0
	RuS_2 (FeS_2)	6	3	0	1
	Rh_2S_3	6	4	0	0
	PdS	4	4	0	0
	PdS_2	4	2	0	1
5d	TaS_2 (MoS_2)	6	3	0	0
	WS_2 (MoS_2)	6	3	0	0
	ReS_2	6	3	0	0
	OsS_2 (FeS_2)	6	3	0	1
	Ir_2S_3	6	4	0	0
	IrS_2 (FeS_2)	6	3	0	1
	PtS	4	4	0	0

⋆ The numbers in parentheses are according to the nomenclature of the *International Tables for X-ray Crystallography*.

with either octahedral- or trigonal-prismatic TM coordination. Here we shall be concerned only with the '2H' polytype with trigonal-prismatic TM environment which is realized in the group Vb and VIb disulphides. TcS_2 and ReS_2 assume a low-symmetry structure which can be interpreted as a transition from the layered to the pyrite structure. Of course there are various other TM–S compounds, but for these dominant structure types we have analysed the trends in the atomic volume, cohesive energies and relative stabilities across the three transition-metal series.

4. Optimization of the crystal structure and of the atomic volume

For all of the 31 TMS listed in table 1 we have minimized the total energy with respect to the volume and shape of the unit cell and to the parameters determining the atomic coordinates, within the constraints of a fixed space group symmetry. For all of the disulphides we have in addition studied the relative stability of the pyrite and layered (MoS_2-type) structures. For all monosulphides we have investigated the possible existence of an NiAs-type phase.

Table 2. Optimized structural parameters for MoS_2-type layered compounds.

		Volume (Å^3/atom)			Axial ratio			Atomic parameter z		
Structure		V_{exp}	V_{GGA}/V_{exp}	V_{LDA}/V_{exp}	Experiment	GGA	LDA	Experiment	GGA	LDA
4d	NbS_2	18.80	1.01	—	3.59	3.53	—	0.125	0.119	—
	MoS_2	17.72	1.03	0.94	3.89	3.97	3.83	0.121	0.126	0.119
5d	TaS_2	19.18	1.01	—	3.65	3.66	—	0.121	0.121	—
	WS_2	17.68	1.02	0.92	3.91	3.98	3.85	0.123	0.125	0.119

4.1. Layered MoS_2-type compounds

The layered MoS_2 structures belong to a family of polytypic structures with close-packed triangular double layers of S with the TM atoms arranged in the trigonal-prismatic holes of the S double layers. In the rhombohedral α-phase the stacking is AABBCC, while in the hexagonal β-phase it is BBCC. TM atoms occupy the 2c positions with coordinates $(1/3, 2/3, 1/4)$, the sulphur atoms the positions 4f with coordinates $(2/3, 1/3, 1/4 + z)$. The closest S–S distances are across the double layer and within the close-packed layers; the interlayer S–S distances are considerably larger and of a van der Waals type. The difference between the short covalent intralayer bonds and the long van der Waals interlayer bonds is set by the axial ratio c/a and the internal parameter z. Our results compiled in table 2 show that the LDA tends to underestimate both the atomic volume and the axial ratio and to overestimate the internal parameter z. The underestimate of the atomic volume reflects the general overbinding trend inherent in the LDA, while the differences in the structural parameters reduce the difference between the intralayer and interlayer distances. Adding non-local exchange–correlation corrections in the form of the GGA leads to a better prediction of the equilibrium volume, albeit with a certain tendency to overcorrect the LDA error. This tendency is more pronounced for the structural parameters c/a and z, which both increase in the GGA. For the nearest-neighbour geometry, these changes go in opposite directions: increasing c/a increases the interlayer distance, while increasing z reduces these distances. Within the LDA we compute, for MoS_2, S–S distances within the S–Mo–S trilayers of 2.83 Å (one neighbour) and 3.11 Å (six neighbours), and interlayer distances of 3.60 Å. Within the GGA the corresponding distances are 3.17 Å/3.17 Å and 3.62 Å, to be compared with the experimental values of 2.98 Å/3.16 Å/3.66 Å. Hence although the GGA leads to a better prediction of the atomic volume, the prediction of the nearest-neighbour geometry is only little affected: we find ratios of $d_3/d_2 = 1.16/1.14/1.16$ (LDA/GGA/experiment) for the relevant interlayer and intralayer distances, and of $d_3/d_1 = 1.27/1.14/1.23$ for the S–S distances between the trilayers and across the trilayer.

The S–S distances within a layer (d_2) are determined by covalent S–S bonds, while the interlayer distance (d_3) depends on the strength of the van der Waals forces holding the S–Mo–S sandwiches together. Hence the good agreement of the ratios d_3/d_2 calculated in the LDA and in the GGA with experiment means that the relative strength of covalent and van der Waals bonds is correctly predicted. The S–S distances across the S–Mo–S trilayers (d_1) depend on the strength of the heterovalent Mo–S interactions. Hence the ratio d_2/d_1 measures the relative strength of homovalent S–S and heterovalent Mo–S interactions. The variation $d_2/d_1 = 1.10/1.00/1.06$ in the series LDA/GGA/experiment indicates that the

Table 3. Optimized structural parameters for pyrite-type compounds.

		Volume (Å^3/atom)			Atomic parameter u			S–S distance (Å)		
Structure		V_{exp}	V_{GGA}/V_{exp}	V_{LDA}/V_{exp}	Experiment	GGA	LDA	Experiment	GGA	LDA
3d	MnS_2	18.83	0.75	—	0.099	0.120	0.123	2.09	2.33	—
	FeS_2	13.33	0.93	—	0.115	0.117	—	2.16	2.20	—
	CoS_2	14.16	0.98	—	0.110	0.115	—	2.11	2.19	—
	NiS_2	14.79	1.01	—	0.106	0.107	—	2.07	2.08	—
4d	RuS_2	14.72	1.02	0.97	0.112	0.113	0.114	2.17	2.21	2.19
5d	OsS_2	14.78	1.02	0.94	0.114	0.116	0.116	2.21	2.26	2.24
	IrS_2	15.27	1.02	—	—	0.132	—	—	2.62	—

weakening of the LDA overbonding arises mainly from adding a repulsive force along the steepest electron-density gradients.

4.2. Pyrite-type compounds

In the cubic pyrite structure the TM atoms occupy the sites of a face-centred cubic lattice and the S atoms are arranged in pairs across the midpoints of the cell edges and the cell centre. The atomic positions are: Fe: 4a (000); S: 8c (uuu); the bond length in the S–S pairs is $d_{S-S} = a(1-2u)\sqrt{3}$; and the shortest TM–TM distances are $d_{TM-TM} = a/\sqrt{2}$. Among the pyrite-type compounds, LDA calculations have been performed only for RuS_2 and OsS_2; see table 3. Again the predicted equilibrium volume is too small (by 3 and 6%, respectively), but since the internal parameter u is slightly underestimated, the shortest S–S distances are correct to within 0.03 Å. The GGA corrects the prediction of the atomic volume (with the notable exception of that for MnS_2; see below); the maximum error is now within 2%. The atomic parameter is little influenced by the non-local corrections; the predicted GGA values tend to be slightly below the experimental values, leading to a small but systematic overestimate of the shortest S–S bond lengths. The TM–TM distances are underestimated in the LDA (especially at lower band filling), but essentially correctly predicted in the GGA. Altogether this means that the characteristic structural parameter d_{TM-TM}/d_{S-S} which increases with the band filling is better predicted in the GGA than in the LDA, e.g. in RuS_2 the ratio is $d_{TM-TM}/d_{S-S} = 1.79/1.81/1.83$ for LDA/GGA/experiment. A striking disagreement with experiment is observed for MnS_2 where even the GGA underestimates the equilibrium atomic volume by as much 25% (the LDA error would be even larger). We shall come back to this point below.

4.3. NiAs-type compounds

In the hexagonal NiAs structure, the As atoms form close-packed layers arranged in a hexagonal stacking sequence; the Ni atoms are located at the centres of all of the octahedral interstices. Hence altogether the stacking sequence is ABCABC with the A layers occupied by Ni, and B and C layers by As. The atomic positions within the unit cell are: Ni: 2a (000); As: 2c $(2/3, 1/3, 1/4)$. Hence the axial ratio c/a is the only free parameter of the structure. Ideal packing is achieved for $c/a = \sqrt{8/3}$, but among the more than fifty binary compounds that are known to assume the NiAs structure, c/a varies from $c/a \leqslant 1.95$ for strongly ionic compounds (the elongation of the cell is thought to be the consequence of the Coulomb

repulsion between the cations which have their shortest distances along the *c*-axis) over nearly ideal values for semiconducting compounds to very small values ($c/a \geqslant 1.27$) for compounds that are generally metallic. For most of the 3d monosulphides, the NiAs phase is stable only in the high-temperature range (but may be maintained at lower temperatures by quenching). VS shows a second-order transition to a MnP-type low-temperature phase [59]. Lattice distortions at lower temperature have been reported also for CrS (LT: monoclinic) [31], FeS (LT: hexagonal [35]), and NiS (LT: rhombohedral) [60]. All 3d monosulphides show antiferromagnetic (AFM) ordering at low temperatures. While CrS, FeS and CoS are AFM metals, in NiAs-type NiS the paramagnetic–antiferromagnetic transition is coupled with a metal–semiconductor transition [61, 62]. An insulating AFM phase is also formed by NaCl-type MnS [63]. The insulating AFM phases of the TM monosulphides are, in analogy with the TM monoxides, most often considered as Mott insulators, although some attempts have been made to reinterpret the insulating behaviour in a one-electron picture [64]. As regards the catalytic activity, the paramagnetic HT phase is of primary interest since the temperature in the reactor is always above the Néel temperature.

Table 4. Optimized structural parameters for NiAs-type compounds.

Structure		Volume (Å^3/atom)			Axial ratio		
		V_{exp}	V_{GGA}/V_{exp}	V_{LDA}/V_{exp}	Experiment	GGA	LDA
3d	VS	13.97	0.95	0.89	1.73	1.92	1.93
	CrS	13.63	0.93	—	1.55	1.82	—
	FeS	14.81	0.83	—	1.67	1.54	—
	CoS	12.69	1.01	—	1.64	1.53	—
	NiS	13.63	1.00	—	1.55	1.53	—
4d	NbS	15.42	1.01	—	1.95	2.03	—

Our results (see table 4) show that even the GGA does not lead to entirely satisfactory results for the 3d monosulphides (the LDA has been used only for VS; the result confirms the expectation that the LDA error is even larger): with low band filling the equilibrium atomic volume is underestimated, and the calculated axial ratio is too large for VS and CrS (the missing link in the series is MnS which crystallizes in the NaCl structure). On the other hand, quite accurate predictions of both volume and axial ratio are achieved for CoS, NiS and the only 4d monosulphide stable in the NiAs structure, NbS. All of the early 3d monosulphides are strongly ionic (electronegativity difference $\Delta x \sim 1.0$) and would hence be expected to assume the NaCl structure where the octahedra of cations surrounding the anions share only edges, rather than the NiAs structure where the octahedra share faces along the *c*-direction. The destabilization of the NaCl phase is generally attributed to the very small ionic radius ratio which would allow for direction anion–anion contacts. In the less symmetric NiAs structure the cation–cation repulsion is reduced by assuming a larger c/a ratio. The underestimation of the density leads directly to the prediction of a too large c/a ratio.

The reason for the modest performance of the local density approximation for the early 3d monosulphides and for MnS_2 is not entirely clear. Possible reasons are magnetic effects, strong electronic correlations, and the frozen-core approximation used in constructing the pseudopotentials. Concerning magnetic effects, Hush and Pryce [65] pointed out very early that for TM ions with more than three and less than eight valence electrons, high-spin and low-spin configurations lead to different distributions of the electrons over the d(t_{2g})

and d(e_g) orbitals and hence to different effective transition-metal radii (with the high-spin configuration leading to larger radii). Hence the high-spin solution is realized for the V, Cr, Mn sulphides and FeS (but not FeS_2). As demonstrated by Oguchi *et al* [64], magnetic fluctuations (finite magnetic moments with random orientations on the TM sites) play an important role even in the paramagnetic phase (although total energy calculations have not been performed). A more detailed analysis using local spin-density calculations will be left to future work. For the early 3d TM the frozen-core approximation is always somewhat problematic. Although the 3p 'semicore' states do not mix with the valence bands, configurations with short interatomic distances can lead to a broadening of the 3p states and make a substantial contribution to the internal pressure. It is well known that the treatment of the 3p states as valence states reduces the DFT error in the prediction of the lattice parameters of the 3d metals with a band that is less than half-filled. Similar studies for the sulphides remain to be done.

Table 5. Optimized structural parameters for tetragonal transition-metal sulphides.

Structure		Volume (Å^3/atom)			Axial ratio			
		V_{exp}	V_{GGA}/V_{exp}	V_{LDA}/V_{exp}	Experiment	GGA	LDA	$\Delta(X_i)_{max}$* (Å)
4d	PdS	17.08	1.04	0.97	1.03	1.03	1.04	0.0026
5d	PtS	18.36	1.06	0.99	1.76	1.86	1.76	—

* The maximal difference in the atomic parameters between experiment and GGA calculations.

Table 6. Optimized structural parameters for trigonal transition-metal sulphides.

	Structure	Volume (Å^3/atom)			Axial ratio			
		V_{exp}	V_{GGA}/V_{exp}	V_{LDA}/V_{exp}	Experiment	GGA	LDA	$\Delta(X_i)_{max}$* (Å)
3d	Cr_2S_3	16.99	0.87	0.79	2.81	2.93	2.93	0.0038
	Ni_3S_2	13.50	1.01	—	1.24	1.24	—	0.0003
	NiS (millerite)	14.00	1.00	—	0.33	0.33	—	0.0160

* The maximal difference in of the atomic parameters between experiment and GGA calculations.

4.4. Tetragonal and trigonal structures

PdS and PtS crystallize in two rather different crystal structures. In the PtS lattice the S atoms occupy the corners of a tetragonally distorted simple cubic lattice, while the Pt atoms occupy the centres of two opposite faces of the cell, alternately in the (100) and (010) planes proceeding in the *c*-direction. Hence the axial ratio is the only free parameter. We find (see table 5) that the LDA leads to a better description of the volume and structure—here the tendency of the GGA to overcorrect the LDA error is particularly pronounced. PdS forms a complex structure in which the Pd atoms form hexagon–triangle nets alternating with triangle–square nets occupied by the S atoms. The structure is usually thought to be controlled by high coordination. We find that LDA and GGA predict the structure to within -3% and $+3\%$, and both the axial ratio and internal structural parameters are described accurately in the GGA (see table 5; only the maximal error $\Delta(X_i)_{max}$ in the calculated parameters X_i is quoted). The trigonal structure of NiS (millerite) consists of triangular

nets of Ni and S alternating along the *c*-direction. The volume and crystal structure (six internal parameters plus the axial ratio) are described accurately in the GGA (see table 6). The trigonal cell of Ni_3S_2 is slightly distorted from a cube; the S atoms form a distorted body-centred cubic array with the Ni atoms located in the centre of the distorted tetrahedral holes (three formula units per cell). Again the volume, axial ratio and all internal parameters are predicted with good accuracy (table 6). The hexagonal cell of Cr_2S_3 (four formula units) contains S atoms in hexagonal close-packed arrays, with the Cr atoms occupying all or one third of the octahedral holes between alternate pairs of S layers. Here we find a 13% underestimate of the equilibrium volume (similarly to the case for all V, Cr and Mn sulphides), although the axial ratio and internal coordinates are predicted accurately (table 6).

Table 7. Optimized structural parameters for miscellaneous compounds (see table 1 for the crystal structures).

		Volume (Å^3/atom)			a^*	b^*	c^*	$\Delta(X_i)_{max}$**
	Structure	V_{exp}	V_{GGA}/V_{exp}	V_{LDA}/V_{exp}	(Å)	(Å)	(Å)	(Å)
3d	FeS (troilite)	15.04	0.85	—	5.822	5.822	10.474	0.0452
					(5.958)	(5.958)	(11.740)	
	MnS	17.99	0.73	0.67	4.719	4.719	4.719	—
					(5.240)	(5.240)	(5.240)	
	FeS_2 (marcasite)	13.53	1.01	—	4.462	5.434	3.395	0.0047
					(4.436)	(5.414)	(3.381)	
	Co_9S_8	14.39	0.98	0.90	9.875	9.875	9.875	0.0032
					(9.928)	(9.928)	(9.928)	
4d	Rh_2S_3	15.54	1.03	0.94	8.525	6.035	6.224	0.0054
					(8.462)	(5.985)	(6.138)	
	PdS_2	18.99	1.00	—	5.570	5.640	7.242	0.0026
					(5.460)	(5.461)	(7.531)	
5d	ReS_2	18.28	1.02	—	6.450	6.391	6.497	0.0041
					(6.417)	(6.377)	(6.461)	
	Ir_2S_3	15.64	1.02	—	8.525	6.051	6.185	—
					(8.465)	(6.011)	(6.149)	

* Lattice parameters calculated with the GGA, with experimental values in parentheses; cf. table 1.
** The maximal difference in the atomic parameters between experiment and GGA calculations.

4.5. Miscellaneous structures

Our results for the remaining sulphides are compiled in table 7. Again we find for MnS and FeS a striking disagreement between the GGA and LDA predictions and experiment. MnS crystallizes in the rock-salt structure, and FeS (troilite) in a complex distorted superstructure of the NiAs structure (which is described only moderately well). The result for FeS contrasts with the excellent structural prediction for the marcasite phase of FeS_2 (cf. also table 3 for FeS_2 in the pyrite phase). The marcasite structure can be derived from the NiAs structure by introducing vacancies in an ordered array. This would suggest that the difficulty is not a fundamental one, but related to the different magnetic properties of the monosulphides and disulphides.

In Co_9S_8 (four formula units per cell) the S atoms form a close-packed cubic array with the Co atoms centring half of the tetrahedral holes and 1/8 of the octahedral holes. We note

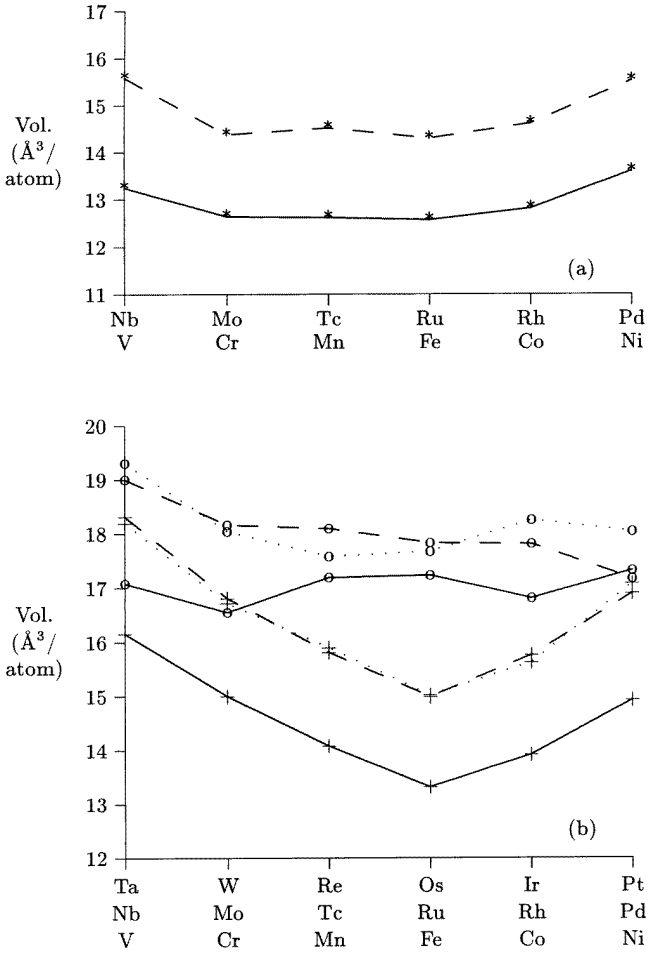

Figure 1. (a) Variation of the atomic volume of the NiAs-type monosulphides as a function of the filling of the d band. Full lines: 3d TMS; dashed lines: 4d TMS. (b) Variation of the atomic volume of the layered (MoS_2-type) and pyrite (FeS_2-type) disulphides as a function of the filling of the d band. Full lines: 3d TMS; dashed lines: 4d TMS; dotted lines: 5d TMS. Asterisks: NiAs; crosses: pyrite; circles: layered.

a large influence from the non-local corrections to the exchange–correlation functional and a very accurate structural prediction in the GGA.

The orthorhombic Rh_2S_3 (and Ir_2S_3) structure (four formula units per cell) contains face-sharing pairs of distorted S octahedra surrounding the Rh atoms. The Rh (Ir) atoms form distorted triangular nets in an arrangement similar to (110) layers in a body-centred cubic structure. Despite the low symmetry, the GGA leads to a very accurate prediction of all structural parameters for both Rh_2S_3 and Ir_2S_3 (table 7). The PdS_2 structure (four formula units per cell) is a distorted pyrite structure with a strongly elongated *c*-axis. The distortions of the cell and of the octahedral and tetrahedral coordinations of Pd and S, respectively, are well described with the GGA.

For ReS_2 the parameters of the triclinic cell and of the internal atomic positions are predicted with good accuracy; see table 7.

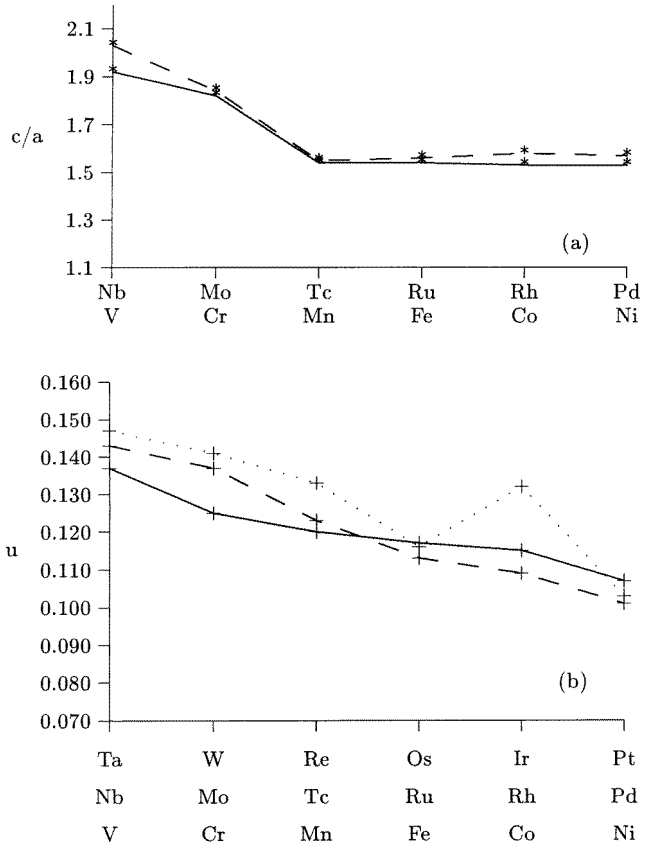

Figure 2. (a) Variation of the axial ratio, c/a, for the NiAs structure versus the band filling. (b) Variation of the atomic parameter, u, for the pyrite structure versus the band filling. (c) Variation of the axial ratio, c/a, for the layered structure versus the band filling. (d) Variation of the atomic parameter, u, for the layered structure versus the band filling. For the explanation of the symbols, see figure 1.

4.6. Structural trends as a function of the filling of the d band

The results discussed in the previous sections allow us to assess the accuracy of the structural predictions based on density functional methods (with the exception of the difficulties relating to the (anti-) ferromagnetic character of certain compounds). To obtain further insight into the mechanisms determining the crystal structures, we performed calculations for all 3d and 4d monosulphides in the NiAs structure and of all 30 disulphides in the pyrite and layered structures to analyse the dependence of the structural parameters on the filling of the TM d band. Figure 1(a) presents the results for the variation of the atomic volume for NiAs-type compounds. For the monosulphides we predict only a weak dependence on the d-band filling with a minimum for a half-filled band, reflecting essentially the trend in the atomic volumes of the transition metals. This is correct for the low-spin paramagnetic materials, but not for the high-spin antiferromagnets (cf. above). For the axial ratio of the NiAs structure, we find very large values for a low band filling, decreasing rapidly towards nearly ideal values for the half-filled band and remaining essentially constant if further d

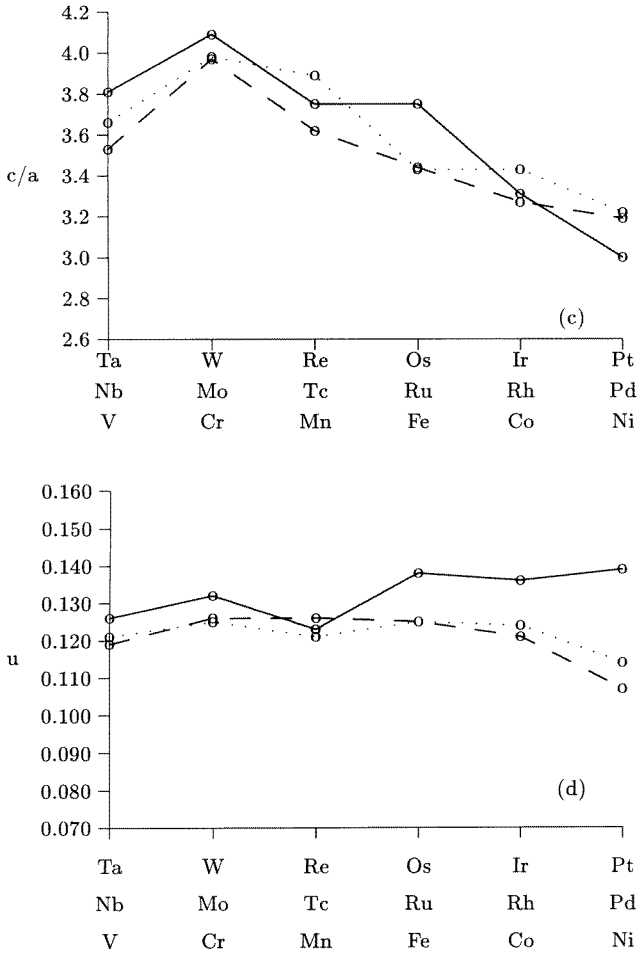

Figure 2. (Continued)

electrons are added (see figure 2(a)). This trend reflects the high ionicity of the 'early'-TM sulphides leading to a strong cation repulsion and hence a large axial ratio (a trend that is actually reinforced by the underestimate of the atomic volume), and the semiconducting character of the 'late'-TM sulphides where a strong directional bonding in the TMS_6 trigonal prisms stabilizes a nearly ideal structure.

In the pyrite structure, the atomic volume decreases continuously to a minimum in the Fe, Ru, Os group and increases again at higher band filling (see figure 1(b)), with only little variation in the internal structural parameter (and hence the S–S distances). This trend is easily understood within a rigid-band picture: the valence bands consist of completely filled S s and S p bands (with some admixture of bonding e_g states), a non-bonding TM t_{2g} band and e_g band—this structure is determined essentially by the octahedral TMS_6 complex [66]. With six d electrons the t_{2g} band is just completely filled; the material is semiconducting and has the maximum bond order. Higher d-band filling leads to an occupation of antibonding states and hence weaker bonding and larger atomic volume. Details of the electronic structure will be given in II. The structural parameter, u, decreases

with increasing band filling (see figure 2(b)) since $d_{S-S} \propto (1 - 2u)$, this means that the bond length in the S pairs increases.

In the layered compounds, the atomic volume shows only little variation across the d series, except for an initial decrease from NbS_2 to MoS_2 and TaS_2 to WS_2, accompanied by an increase of the axial ratio (which decreases again at higher d-band filling; see figure 2(c)). This means that in a stable layered compound the ratio of the thickness of the S–TM–S sandwich to the interlayer distance is essentially constant. Again the trend may be interpreted in a rigid-band picture [67]: the occupied part of the valence bands is made up by completely filled S s and S p bands, followed by a narrow TM d band exactly at the Fermi level. This band is of predominantly $d_{3z^2-r^2}$ character at Γ and $d_{x^2-y^2}$, d_{xy} character at the Brillouin-zone boundary. The band contains two electrons; it is separated by a gap from a broad d band containing eight electrons (for details see II and also the early non-self-consistent calculations by Mattheis [68]). For NbS_2 and TaS_2, the two-electron band is just half-filled, and the TM d–S p bonds are weak. In MoS_2 and WS_2 the d–p band bonds are completely saturated. The internal parameter u shows only a small variation over the range of the d-band filling where the layered structure is stable (cf. figure 2(d)).

5. Cohesive energies

The cohesive energy is defined as the difference between the total energy per atom in the compound and the weighted average of the total energies of the free atoms. For sulphur, the electronic configuration of the free atom is clearly s^2p^4, but for the transition-metal atoms, the total energy must be minimized with respect to the electronic configuration and the spin configuration, both in the LDA and GGA. This has been done using the spin-polarized version of VASP; for details, see Moroni *et al* [28]. The experimental cohesive energies have been calculated from the heats of formation of the compounds and the heats of sublimation of the elements, using standard values [69].

The calculated values of the cohesive energies are compiled in table 8. The most striking result is that the LDA tends to overestimate the cohesion by 25 to 30%, on average (considering the spin corrections for the free atoms; without these corrections, taking a non-spin-polarized $d^{n-1}s^1$ standard electron configuration for the TM atoms, the overbinding can be as large as 60%). The gradient corrections eliminate the trend to overbinding; on average the calculated cohesive energies are accurate to within 5% with the exception of the difficult 3d sulphides (V, Cr, Mn) noted in connection with the atomic volume. Again the spin corrections for the free atoms are very important (27% on average in the GGA).

5.1. Trends with d-band filling—relative stabilities of pyrite and layered structures

Figure 3 represents the variation of the calculated cohesive energies for all stable and hypothetical TM disulphides. In all three series, the layered structure is more stable for low band filling: this is correct for the Nb, Mo, Ta and W disulphides, but for V and Cr layered disulphides do not exist, although they are predicted to be more stable than the pyrite-type compounds. Here the competition with compounds with a different stoichiometry has to be examined. The crossover from the layered to the pyrite structure occurs for five d electrons. This is probably correct for the 4d and 5d series, but for both TcS_2 and ReS_2 a triclinic structure is lower in energy. For ReS_2 the energy difference is by 0.31 eV/atom. For d bands that are more than half-filled the pyrite-type compounds are predicted to be more stable than the layered phases. This agrees with the experimental data for the 3d disulphides (FeS_2, CoS_2, NiS_2) and for RuS_2 in the 4d series and OsS_2, IrS_2 in the 5d series. For FeS_2, we

Table 8. Cohesive energies of the transition-metal sulphides (in eV/atom).

	Structure	E_{exp}	E_{GGA}	E_{GGA}/E_{exp}	E_{LDA}/E_{exp}
3d	VS	5.61	5.02	0.90	1.12
	Cr_2S_3	4.79	3.81	0.80	1.06
	CrS	—	4.09	—	—
	MnS	4.03	4.03	1.00	1.12
	FeS (NiAs)	4.14	4.42(6)	1.07	—
	FeS (troilite)	—	4.43(5)	—	—
	FeS_2 (pyrite)	3.92	4.29	1.08	—
	FeS_2 (marcasite)	3.92	4.31	1.10	—
	Co_9S_8	4.23	4.91	1.15	1.44
	CoS	4.10	4.68	1.14	—
	Ni_3S_2	4.30	4.54	1.06	—
	NiS (millerite)	4.12	4.39	1.07	—
	NiS (NiAs)	—	4.32	—	—
	NiS_2	—	4.02	—	—
4d	NbS	—	6.16	—	—
	NbS_2	5.68	5.54	0.98	—
	MoS_2	5.18	5.11	0.99	1.21
	RuS_2	4.88	5.05	1.03	1.28
	Rh_2S_3	4.61	4.84	1.05	1.29
	PdS	3.80	3.76	0.99	1.26
	PdS_2	—	3.60	—	—
5d	TaS_2	5.87	6.04	1.03	—
	WS_2	5.78	5.78	1.00	1.20
	ReS_2	5.23	5.35	1.02	—
	OsS_2	5.19	5.34	1.03	1.26
	Ir_2S_3	5.06	5.37	1.06	—
	IrS_2	4.77	5.07	1.06	—
	PtS	4.83	4.69	0.97	1.20

have also explored the relative stability of the marcasite structure (stable at low temperature) and the pyrite structure (stable at higher temperatures). We find the marcasite form to be lower in energy by 20 meV/atom (see table 8), in agreement with the observed stabilities. At the end of the 4d and 5d series, however, where the cohesive energy decreases steeply, the competition with sulphides of different stoichiometry must be explored to understand the absence of stable pyrite-type compounds.

5.2. Relative stability of monosulphide structures

Among the monosulphides the most frequent structure is the NiAs type. In the 3d series, monosulphides exist through the entire series. At the beginning of the series (VS, CrS), the NiAs phase is stable. For MnS we fail to predict the stability of the NaCl structure relative to the NiAs type. At higher d-band filling, the NiAs phase competes with the low-temperature phase of lower symmetry (troilite in FeS, millerite in NiS) or with off-stoichiometric phases (CoS versus Co_9S_8) (see table 1). For FeS, we predict the troilite phase to be 9 meV/atom lower in energy than the NiAs phase (see table 8), in agreement with its low-temperature stability. A similar result is obtained for NiS, where the millerite phase is energetically more favourable by about 70 meV/atom. For the CoS system a homogeneous NiAs-type compound exists only at high temperature, whereas at low temperature the Co_9S_8 phase is

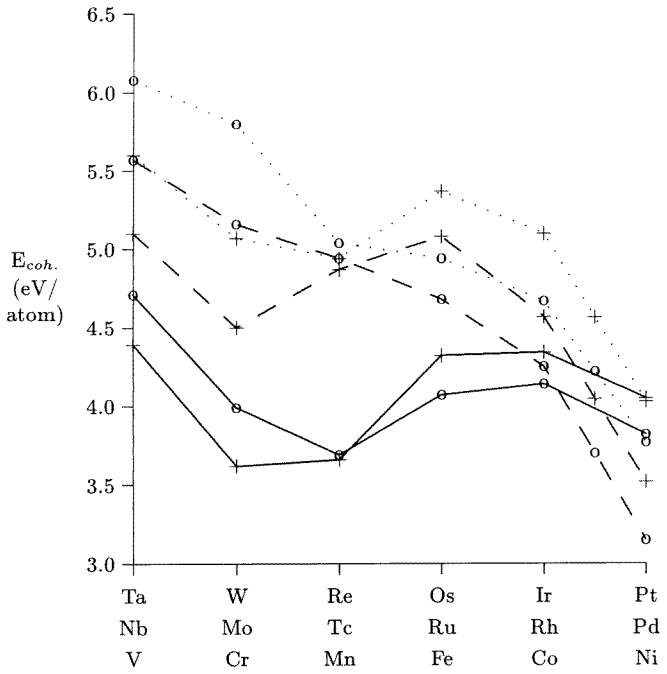

Figure 3. Variation of the cohesive energies as a function of the filling of the d band for all 3d, 4d, and 5d disulphides in the layered and pyrite structures. For the explanation of the symbols, see figure 1.

stabilized. This agrees with our prediction of a total energy that is lower by 0.12 eV/atom in the off-stoichiometric phase.

Among the 4d and 5d monosulphides, an NiAs-type phase is formed only in NbS, while PdS and PtS assume tetragonal phases. Here the problem is evidently the relative stability of phases of different composition.

5.3. Relative stability of monosulphides and disulphides

The coexistence of monosulphides and disulphides throughout the 3d series contrasts with the singular appearance of monosulphides in the 4d and 5d series (only NbS, PdS and PtS). To explore this interesting correlation, we have to compare the enthalpies of formation, ΔH_f, as a function of the composition. The stable TMS must fall on a complex polygon. This is a first step towards the determination of the low-temperature limit of the phase diagram. Of course, such a study would—in principle—include TMS of all possible stoichiometries, but this is clearly excluded because of the immense computational effort required and also because of incomplete structural information. Figure 4 shows the ΔH_f versus composition diagram for the Fe, Co and Ni sulphides. Only the monosulphides and disulphides exist in the Fe–S system. However, we find that the enthalpies of formation of the NiAs and troilite phases of FeS lie above the straight line connecting pure Fe and FeS_2. Hence our calculation predicts FeS to be unstable—this is clearly related to the magnetism of the Fe-rich compounds. For CoS, the stable low-temperature phases are Co_9S_8 and CoS_2, whereas the monosulphide exists only above about 735 K, possibly with Co vacancies [70].

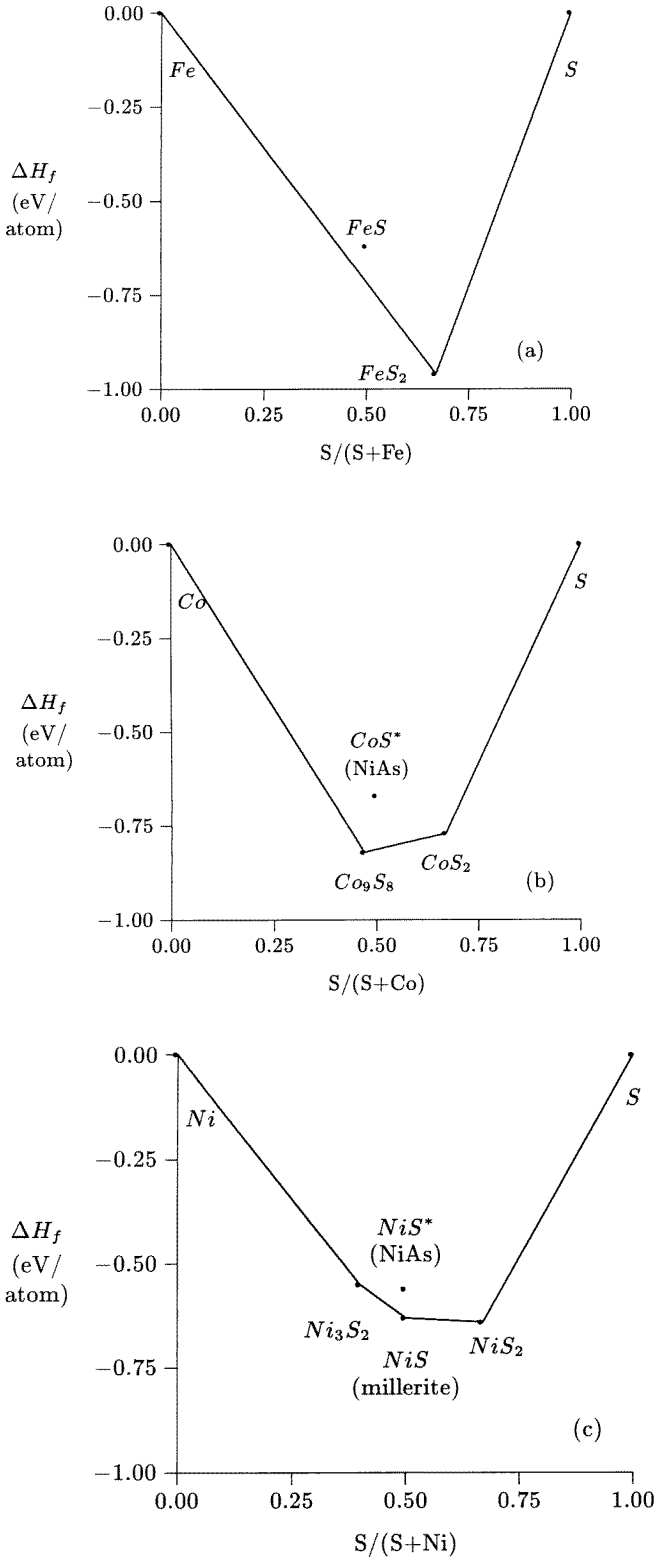

Figure 4. Enthalpy of formation versus composition for the Fe–S (a), Co–S (b), Ni–S (c) systems. High-temperature phases are labelled with an asterisk; cf. the text.

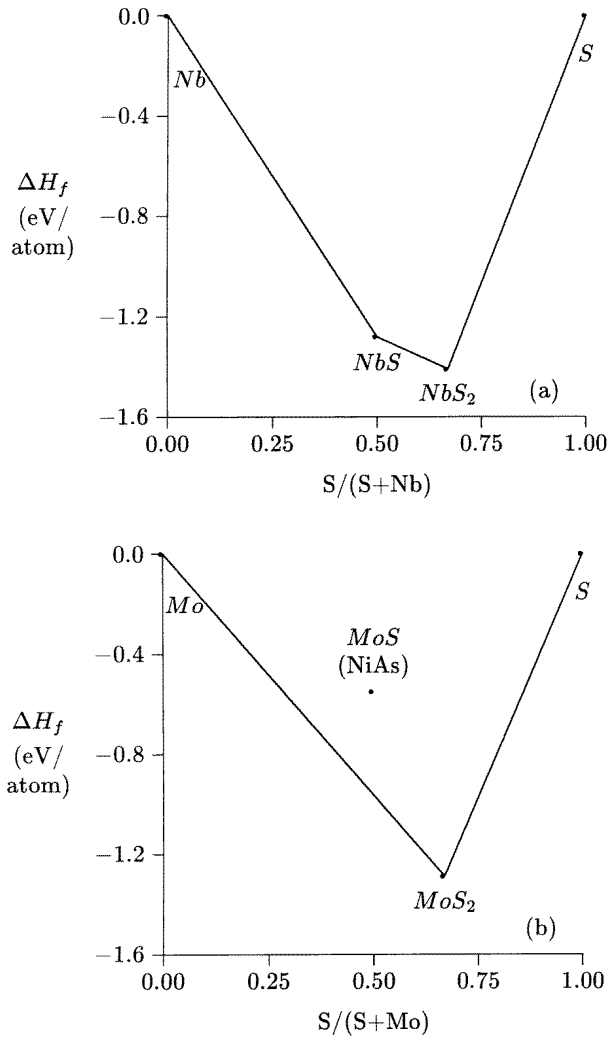

Figure 5. Enthalpy of formation versus composition for the Nb–S (a), Mo–S (b), Rh–S and Ir–S (c), and Pd–S (d) systems; cf. the text.

This agrees with the calculated enthalpies of formation (see figure 4(b)). Sulphides with compositions Co_4S_3 and Co_3S_4 have not been included in the analysis because of incomplete structural information. The calculated enthalpies of formation for the Ni sulphides confirm the low-temperature stability of Ni_3S_2, NiS (millerite, but not the NiAs polymorph) and NiS_2. Again some intermediate phases have been omitted.

The corresponding diagrams for some of the 4d TMS are compiled in figure 5. For the Nb–S system, the coexistence of the NiAs-type monosulphide and the layered disulphide is clearly established, while in the Mo–S system the monosulphide is unstable, in agreement with experiment. At the end of the 4d series, our calculations confirm the coexistence of Rh_2S_3 and RhS_2 (the Rh defects mentioned in the experimental reports have been ignored [58]). The phase diagram also shows further phases of composition $Rh_{17}S_{15}$ and Rh_3S_4 which could not be treated because of incomplete structural information. Very similar

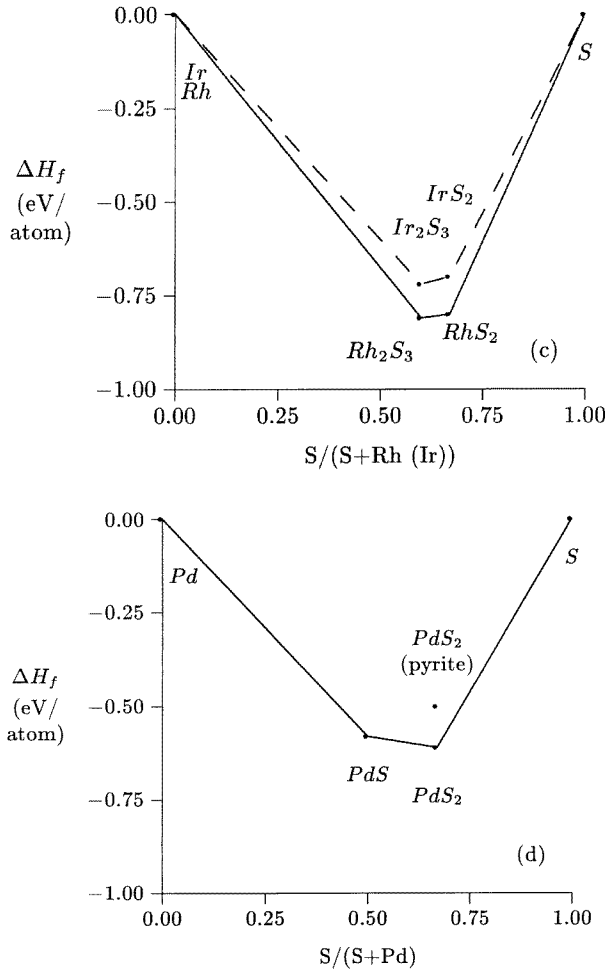

Figure 5. (Continued)

results have been obtained for the homologous Ir–S system where the existence of a pyrite-type disulphide is not undisputed. Finally for the Pd–S systems our calculations correctly predict the coexistence of PdS and PdS_2, both in prototypic structures (with relatively large structural energy differences relative to the more common NiAs and pyrite structures: $\Delta E(\mathrm{PdS}) = -0.28$ eV/atom, $\Delta E(\mathrm{PdS_2}) = -0.10$ eV/atom).

6. Metal–sulphur bond strength versus catalytic activities

In the preceding sections we have shown that LDA + GGA calculations allow one to access the structural and cohesive properties of TMS with good accuracy. We now turn to a very brief and preliminary discussion of the fundamental significance of the TM–S bond strength for the catalytic activity of transition-metal sulphides in hydrodesulphurization. From table 1, we see that in the majority of the TMS, the TM atoms are surrounded only by sulphur atoms and vice versa. In this case, we can estimate the strength of the bond as the cohesive

energy per formula unit, divided by the number of TM–S bonds. The exceptions are the Ni_3S_2 and NiS (millerite) phases where there are a substantial number of metal–metal bonds and the pyrite structure where S_2 pairs exist. In this case we assume that the S–S and TM–S bonds have comparable strength.

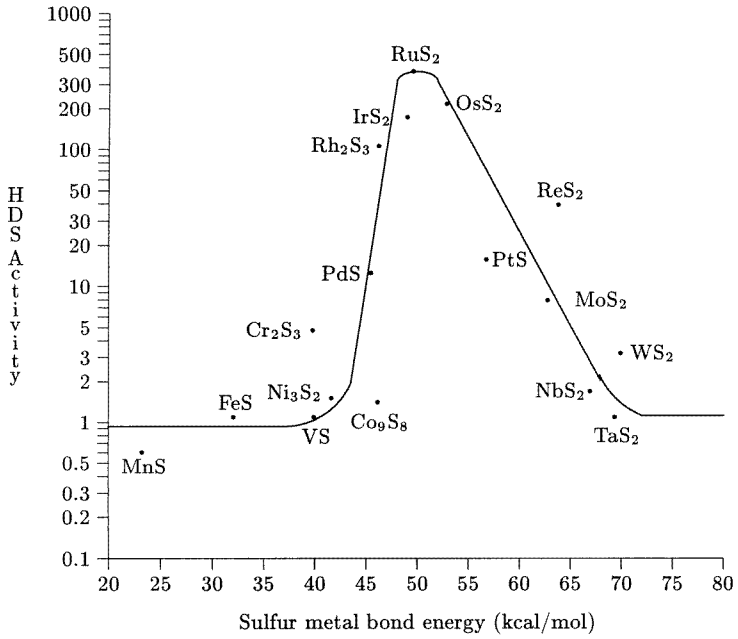

Figure 6. Variation of the HDS activity of the TMS catalysts (in molecules of dibenzothiophene converted per millimole of metal per second $\times 10^{16}$ as measured by Pecoraro and Chianelli [1]) as a function of the metal–sulphur bond energy defined as the cohesive energy per TM–S bond (or per TM–S and S–S bond for the pyrite structures; cf. the text) and calculated under the GGA approximation with VASP.

Figure 6 shows the catalytic activity for hydrodesulphurization (as measured by Pecoraro and Chianelli [1]) against the TM–S bond strength calculated in our work. The result is a clear illustration of the Sabatier principle discussed in the introduction: TMS with too high and too low TM–S bond strength possess only a low catalytic activity. Admittedly, this correlation could have been established on the basis of the experimental cohesive energies or heats of formation as well. We include here this result to demonstrate that the calculated total energies are sufficiently accurate to display this important relation, reported for the first time and more extensively discussed in reference [5].

7. Conclusions

We have presented density functional calculations of the structural and cohesive properties of a large number of transition-metal sulphides of technological interest for applications in catalysis. Our results demonstrate that in the local density approximation there is a quite pronounced trend towards an overbinding which manifests itself in the prediction of too small atomic volumes and too large cohesive energies. Non-local corrections to the exchange–correlation functional in the form of a generalized-gradient approximation lead

to a very accurate prediction of the cohesive energies, but for the atomic volumes there is a certain tendency to overcorrect the LDA error which is most pronounced for the sulphides of the heavy transition metals. Problems are identified for the sulphides of the early 3d series (V–S, Cr–S, Mn–S) where the magnetism of the sulphides will have to be taken into account.

We have also performed very detailed optimizations of the crystalline structures demonstrating the ability of the LDA + GGA to predict even very complex structures with high accuracy, and detailed studies of the relative stability of various crystalline polymorphs.

Our calculations demonstrate that total energy calculations made on the basis of the LDA + GGA are sufficiently accurate to establish correlations with the catalytic activities of the transition-metal sulphides. The following paper of this series will present a comprehensive study of the electronic properties of these materials. An extension of the density functional calculations to the surfaces of the transition-metal sulphides and the adsorption of small molecules will be published shortly [71].

Acknowledgments

This work was performed within the Groupement de Recherche Européen 'Dynamique Moléculaire Quantique Appliquée à la Catalyse et à l'Adsorption' supported by the French Centre National de la Recherche Scientifique (CNRS) and the Institut Français du Pétrole.

References

[1] Pecoraro T A and Chianelli R R 1981 *J. Catal.* **67** 430
[2] Harris S and Chianelli R R 1984 *J. Catal.* **86** 400
Harris S and Chianelli R R 1986 *J. Catal.* **98** 17
[3] Topsoe H, Clausen B S and Massoth F 1996 Hydrotreating catalysis *Catalysis (Springer Series in Science and Technology 11)* (Berlin: Springer)
[4] Norskov J K, Clausen B S and Topsoe H 1992 *Catal. Lett.* **13** 1
[5] Toulhoat H, Raybaud P, Kasztelan S, Kresse G and Hafner J 1997 *Symp. on Advances and Applications of Computational Chemical Modelling to Heterogeneous Catalysis (San Francisco, CA, 1997)* (New York: American Chemical Society) at press
[6] Sabatier P 1911 *Ber. Deutsch. Chem. Ges.* **44** 1984
[7] Boudart M 1961 *Chem. Eng. Prog.* **57** 33
[8] Hohenberg P and Kohn W 1964 *Phys. Rev.* B **136** 864
Kohn W and Sham L J 1965 *Phys. Rev.* **140** A1133
Kohn W 1985 *Highlights of Condensed Matter Theory* ed M P Tosi, M Fumi and F Bassani (Amsterdam: North-Holland)
[9] Jones R O and Gunnarsson O 1989 *Rev. Mod. Phys.* **61** 689
[10] Perdew J P, Chevary J A, Vosko S H, Jackson K A, Pedersen M R, Singh D J and Fiolhais C 1992 *Phys. Rev.* B **46** 6671
[11] Kresse G and Hafner J 1993 *Phys. Rev.* B **47** 588
[12] Kresse G and Hafner J 1994 *Phys. Rev.* B **49** 14 251
[13] Kresse G and Furthmüller J 1996 *Comput. Mater. Sci.* **6** 15
[14] Kresse G and Furthmüller J 1996 *Phys. Rev.* B **54** 11 169
[15] Perdew J P and Zunger A 1981 *Phys. Rev.* B **23** 5048
[16] Mermin N D 1965 *Phys. Rev.* **137** A1141
[17] Vanderbilt D 1990 *Phys. Rev.* B **41** 7892
[18] Kresse G and Hafner J 1994 *J. Phys.: Condens. Matter* **6** 8245
[19] Eichler A, Hafner J, Furthmüller J and Kresse G 1996 *Surf. Sci.* **346** 300
[20] Stadler D, Wolf W, Podloucky R, Kresse G, Furthmüller J and Hafner J 1996 *Phys. Rev.* B **54** 1729
[21] Wood D M and Zunger A 1985 *J. Phys. A: Math. Gen.* **18** 1343
[22] Bylander D M and Kleinman L 1992 *Phys. Rev.* B **46** 9837
[23] Payne M C, Teter M P, Allan D C, Arias T A and Joannopoulos J D 1992 *Rev. Mod. Phys.* **64** 1045

[24] Pulay P 1980 *Chem. Phys. Lett.* **73** 393
[25] Jepsen O and Anderson O K 1971 *Solid State Commun.* **9** 1763
[26] Methfessel M and Paxton A T 1989 *Phys. Rev.* B **40** 3616
Methfessel M and Paxton A T 1971 *Phys. Rev.* B **9** 1763
[27] Blöchl P, Jepsen O and Andersen O K 1994 *Phys. Rev.* B **49** 16 223
[28] Moroni E, Kresse G and Hafner J 1997 *Phys. Rev.* B at press
[29] Biltz W and Koecher A 1939 *Z. Anorg. Allg. Chem.* **241** 324
[30] Vaidya N 1976 *Indian J. Pure Appl. Phys.* **14** 600
[31] Jellinek F 1957 *Acta Crystallogr.* **10** 620
[32] Ott H 1926 *Z. Kristallogr., Kristallgeom., Kristallphys., Kristallchem.* **63** 222
[33] Chattopadhyay T, von Schnering H G, Stansfield R F D and McIntyre G J 1992 *Z. Kristallogr.* **199** 13
[34] Coey J M D and Roux-Buisson H 1979 *Mater. Res. Bull.* **14** 711
[35] Bertaut E F 1956 *Bull. Soc. Fr. Minéral. Cristallogr.* **79** 276
[36] Finklea S, Leconte C and Amma E 1976 *Acta Crystallogr.* B **32** 529
[37] Buerger M J 1931 *Am. Mineral.* **16** 361
[38] Geller S 1962 *Acta Crystallogr.* **15** 1195
[39] Schönberg 1954 *Acta Metall.* **2** 427
[40] Nowack E, Schwarzenbach D, Gonschorek W and Hahn T 1989 *Z. Kristallogr.* **186** 213
[41] Parise J B 1980 *Acta Crystallogr.* B **36** 1179
[42] Kolkmeijer N H and Moesvelt A L Th 1931 *Z. Kristallogr., Kristallgeom., Kristallphys., Kristallchem.* **80** 91
[43] Fujii T, Tanaka K, Marumo F and Noda Y 1987 *Mineral. J. Japan* **13** 448
[44] Schönberg N 1954 *Acta Metall.* **2** 247
[45] Jellinek F, Brauer G and Müller H 1960 *Nature* **185** 376
[46] Bronsema K D, De Boer J L and Jellinek F 1986 *Z. Anorg. Allg. Chem.* **540** 15
[47] Wildervanck J C and Jellinek F 1971 *J. Less-Common Met.* **24** 73
[48] Lutz H D, Mueller B, Schmidt T and Stingl T 1990 *Acta Crystallogr.* C **46** 2003
[49] Parthé E, Hohnke D and Hulliger F 1967 *Acta Crystallogr.* **23** 832
[50] Brese N E, Squattrito P J and Ibers J A 1985 *Acta Crystallogr.* C **41** 1829
[51] Grovold F and Rost E 1957 *Acta Crystallogr.* **10** 329
[52] Meetsma A, Wiegers G A, Haange R J and de Boer J L 1990 *Acta Crystallogr.* C **46** 1598
[53] Schutte W J, De Boer J L and Jellinek F 1987 *J. Solid State Chem.* **70** 207
[54] Kelty S P *et al* 1994 *J. Am. Chem. Soc.* **116** 7857
[55] Stingl Th, Mueller B and Lutz H D 1992 *Z. Kristallogr.* **202** 161
[56] Munson R A 1968 *Inorg. Chem.* **7** 832
[57] Bannister F A and Hey M H 1932 *Mineral. Mag. J. Mineral. Soc.* **23** 188
[58] Foise J, Kim K, Covino J, Dwight K, Wold A, Chianelli R and Passaretti J 1983 *Inorg. Chem.* **22** 61
[59] Franzen H F and Wiegers G A 1975 *J. Solid State Chem.* **13** 114
[60] Trahan J, Goodrich R G and Watkins S F 1970 *Phys. Rev.* B **2** 2859
[61] Sparks J T and Komoto T 1967 *Phys. Lett.* **25A** 398
[62] Barker A S and Remeika J P 1974 *Phys. Rev.* B **10** 987
[63] Smart J S 1963 *Magnetism* vol 3, ed G T Rado and H Suhl (New York: Academic) p 63
[64] Oguchi T, Terakura K and Williams A R 1983 *Phys. Rev.* B **28** 6443
[65] Hush N and Pryce M H L 1958 *J. Chem. Phys.* **28** 244
Hush N and Pryce M H L 1958 *J. Chem. Phys.* **26** 143
[66] Bullett D W 1982 *J. Phys. C: Solid State Phys.* **15** 6163
[67] Kertesz M and Hoffmann R 1984 *J. Am. Chem. Soc.* **106** 3453
[68] Mattheis L F 1973 *Phys. Rev.* B **8** 3719
[69] *Handbook of Chemistry and Physics* 1995 75th edn, ed R C Weast (Boca Raton, FL: Chemical Rubber Company Press)
[70] The information on the phase diagrams has been drawn from the compilations of
Hansen M and Anderko K 1958 *Constitution of Binary Alloys* (New York: McGraw-Hill)
Elliot R P (ed) 1961 *Constitution of Binary Alloys* 1st Suppl. (New York: McGraw-Hill)
Shunk F A (ed) 1964 *Constitution of Binary Alloys* 2nd Suppl. (New York: McGraw-Hill)
Moffatt W G (ed) *Handbook of Binary Phase Diagrams* (Schenectady, NY: Genum)
[71] Raybaud P, Kresse G, Hafner J and Toulhoat H 1997 at press